RSC Advances

PAPER

View Article Online
View Journal | View Issue

Cite this: *RSC Adv.*, 2016, **6**, 107768

# $WS_2$–3D graphene nano-architecture networks for high performance anode materials of lithium ion batteries†

Yew Von Lim,[a] Zhi Xiang Huang,[ab] Ye Wang,[a] Fei Hu Du,[a] Jun Zhang,[c] Tu Pei Chen,[c] L. K. Ang[a] and Hui Ying Yang*[a]

Received 23rd August 2016
Accepted 4th November 2016

DOI: 10.1039/c6ra21141k

www.rsc.org/advances

$WS_2$ nanoflakes were grown on three-dimensional graphene networks (3Dgn) synthesized *via* a simple chemical vapor deposition (CVD) method. As anode materials for lithium-ion battery applications, the 3Dgn network not only provides robust mechanical support for the $WS_2$ nanostructure, but also enhances its conductivity and ionic kinetics, leading to an overall improvement in electrochemical performance of $WS_2$ compared to the commercial $WS_2$ powder. The $WS_2$–3Dgn nanocomposites can deliver reversible capacities of 927 and 416 mA h $g^{-1}$ at current densities of 100 and 1500 mA $g^{-1}$, respectively. At current density of 200 mA $g^{-1}$, $WS_2$–3Dgn nanocomposites can retain a capacity of 748 mA h $g^{-1}$ after 500 cycles with Coulombic Efficiency (CE) higher than 98%, indicating outstanding cycling stability. The improved electrochemical performance is attributed to the synergistic effect between the $WS_2$ nanoflakes and the highly conductive 3Dgn network as well as their rationally designed nano-architecture. These results demonstrate a feasible and simple method to synthesize $WS_2$ based hybrid nanocomposites on 3Dgn for next generation high performance LIBs electrode materials.

## 1. Introduction

Lithium-ion batteries (LIBs) are among the most popular and utilized renewable energy power sources due to high energy densities, long cycling stability and the virtually non-existent memory effect.[1–10] As of now, graphite has been mostly used as the commercial anode material due to its stable cycling performance and natural abundance.[11,12] However, the theoretical specific capacity of the graphite is only 372 mA h $g^{-1}$. It is still too low to be utilized as large scale LIBs for high power consumption such as electrical vehicles usage. With the rising demand of electrical vehicles with long lasting performance, it is of great urgency to investigate alternative electrode materials that can provide outstanding electrochemical performance, *i.e.* excellent rate capability and long cycling performance.[13]

Two-dimensional transition metal dichalcogenides, for example the transition metal disulfides (TMDs), have recently received extensive research attention as the anode materials for next generation LIBs as well as supercapacitors.[14,61–64] Compared to the usually studied metal oxides,[15,63] the volume change of layered structure TMDs is much smaller, owing to the weak van der Waals interactions between the layers and its large interlayer spacing.[16] Additionally, the electronic conductivity of TMDs is usually higher than that of metal oxides. *i.e.* $Li_2S$ matrix is generated during the lithiation process to accommodate the metal nanoparticles for TMDs, whereas $Li_2O$ is generated for metal oxides. The conductivity of $Li_2S$ matrix is usually higher than that of $Li_2O$ implying better performance of the TMDs based electrode materials.[17,18] Indeed, recent studies have shown that the TMDs-based electrode materials exhibit superior reversible capability with high specific capacity.[19,20,61,62,65] Tungsten disulfide ($WS_2$), one of the 2D layered structured TMDs, has been identified as one of the candidates for anode material with a theoretical specific capacity of 433 mA h $g^{-1}$, and large interlayer spacing with weak van der Waals interactions.[21] These factors indicate the potential of long cycle stability with high specific capacity of the $WS_2$ based LIBs electrodes.[22]

The general strategies usually adopted to enhance the electrochemical performance of the TMDs structure to accommodate the rapid charging/discharging process of LIBs include (a) incorporation of conductive carbonaceous materials, such as reduced graphene oxide (rGO), carbon nanotubes (CNT), amorphous carbon *etc.*[23–27,63]; (b) controlling the morphology of nanostructures to tailor the surface kinetics between lithium ions and the active materials.[28,29] Majority of research interests have been focused on the usage of graphene oxides (GO) and

[a]*Pillar of Engineering Product Development, Singapore University of Technology and Design, 8 Somapah Road, Singapore 487372, Singapore. E-mail: yanghuiying@sutd.edu.sg; Fax: +65 6779 5161; Tel: +65 6303 6663*

[b]*Airbus Group Innovations Singapore, 110 Seletar Aerospace View, Singapore, 77562*

[c]*School of Electrical and Electronic Engineering, Nanyang Technological University, Singapore, 639798*

† Electronic supplementary information (ESI) available. See DOI: 10.1039/c6ra21141k

rGO due to their facile synthesis methods. However, the conductivity of GO or rGO is still not high enough due to the abundant of defects, oxygen-containing functional groups and grain boundaries within the GO structure.[30] 3D graphene networks (3Dgn) is a connective network of multiple graphene sheet layers grown on nickel foam substrate *via* chemical vapor deposition (CVD) method.[31] The 3Dgn has a unique structure with three dimensional porous and hollow structure different from normal graphene. This inter-connective 3Dgn network has high surface area to volume ratio, suggesting potentially remarkable energy storage potentials.[32,33] It is noteworthy that 3Dgn can also potentially improves electrical conductivity and provides a solid structural backbone for prevention of structural pulverization during lithiation/delithiation processes. In addition, 3Dgn structure can also prevents the restacking issue during the lithiation/delithiation processes which are commonly an issue for graphene and graphene oxide.[34] However, it should be noted that as the surface of 3Dgn is inert and very stable, this results in difficulty to decorate 3Dgn with other nanoparticles for further application.[35] To resolve this issue, the surface of the unreactive and inert graphene can be functionalized or activated by chemical reaction,[36,37] photochemical,[38] thermal[39] and plasma activation methods.[40] Among these activation methods, plasma treatment and activation is a rapid, dry and scalable technique.[40] Without chemical contamination, plasma treatment can effectively modify the surface kinetics and generate large amount of surface defects and dangling bonds on the surface of 3Dgn for further rational loading of the effective active materials. Therefore plasma activation on graphene prior to active material growth provides an attractive method to achieve (i) repeatable and scalable growth control mechanism of nanostructure, and (ii) enhancement in electrochemical performance of active materials.

Herein, we have successfully synthesized nanocomposites of $WS_2$ nanoflakes on 3Dgn of which the 3Dgn were pre-activated with plasma treatment in various times before the CVD growth of $WS_2$ nanoflakes. This is the first time plasma treatment is utilized to modify the surface kinetics of 3Dgn for $WS_2$ nanoflakes decoration until rational loading with active materials is reached to achieve the best electrochemical performance. The $WS_2$–3Dgn nanocomposites exhibit exceptional capacity and stable cyclic performance as the anode materials of LIBs. Significantly, it can deliver a specific capacity of 927 and 416 mA h $g^{-1}$ at current density of 100 and 1500 mA $g^{-1}$ respectively. It is also able to retain a specific capacity of 748 mA h $g^{-1}$ at a current density of 200 mA $g^{-1}$ even after 500 cycles. The improved electrochemical performance is attributed to the synergistic effect between the $WS_2$ nanoflakes and 3Dgn network, and also to the special designed structure of the hybrid nanocomposites.

## 2. Experimental details

### 2.1 Synthesis of the $WS_2$–3Dgn nanocomposites

3Dgn was grown on nickel foam based on the previously reported method with slight modifications.[41] Nickel foam substrates was heated to 1000 °C with a ramping rate of 20 °C $min^{-1}$ in forming gas ($N_2 : H_2 = 95\% : 5\%$) environment within a tube furnace CVD chamber. Anhydrous reagent alcohol (from Sigma-Aldrich) vapor was bubbled and introduced into the CVD chamber when the temperature was increased to 1000 °C and kept for 10 min for 3Dgn growth. After that, the furnace was allowed to cool down rapidly with a rate of approximately 100 °C $min^{-1}$ to room temperature by subjecting the setup to table fan cooling. The resultant mass loading of 3Dgn is about 0.20 mg $cm^{-2}$.

$WS_2$ precursor solution was prepared by dissolving ammonium tetrathiotungstate ($(NH_4)_2WS_4$, Sigma-Aldrich) in *N*,*N*-dimethylmethanamide (DMF, Sigma-Aldrich) with concentration of 100 mmol $l^{-1}$. Nickel foam substrates with 3Dgn grown on top were tailored into 1 $cm^2$ pieces and subjected to air plasma treatment for various duration times to functionalize the 3Dgn surface for catalyzing subsequent growth of $WS_2$ nanostructure. The plasma treated 3Dgn samples were dip-casted in the precursor solution for 10 min and baked at 90 °C for 120 min. The resultant samples were then transferred to the CVD chamber and heated to 700 °C in a ramping rate of 5 °C $min^{-1}$ and kept for 60 min in the forming gas environment.[42] The chamber was cooled down to room temperature naturally within the same gas ambient. The mass loading of $WS_2$–3Dgn nanocomposites with various plasma treatment times are shown in Table 1. The samples treated by plasma with 30, 60 and 90 s are named as 30WSG, 60WSG and 90WSG, respectively.

### 2.2 Materials characterization

The morphologies of all samples were studied by using field emission scanning electron microscopy (FESEM, JEOL Japan JSM-7600F) and transmission electron microscopy (TEM, JEOL Japan, JEM-2010). The crystal structure studies of the all samples was carried out *via* X-ray diffraction (XRD, Bruker D8 Advance) using the Cu K$\alpha$ ($\lambda = 0.154$ nm) radiation lines with the accelerating voltage of 40.00 kV. Raman spectroscopy was performed on WITec Instruments confocal Raman system (WITec Instruments. Alpha-300R, Germany) with 532 nm laser as excitation source.

### 2.3 Electrochemical performance evaluation

All electrochemical performance testing and measurements were carried out based on a half-cell two electrode configuration. In a typical configuration, pure lithium metal foil was used as the counter electrode, and $WS_2$–3Dgn nanocomposites as the working electrode. The $WS_2$–3Dgn nanocomposites were

Table 1 Mass loadings the $WS_2$–3Dgn composites with various plasma durations, control sample of 3Dgn and bulk $WS_2$ powder electrodes

| Name | Plasma treated time (s) | Mass loadings (mg $cm^{-2}$) |
|---|---|---|
| Bulk $WS_2$ | — | ~2.0 |
| 3Dgn | — | ~0.2 |
| 30WSG | 30 | 0.3–0.5 |
| 60WSG | 60 | 0.7–1.1 |
| 90WSG | 90 | 1.5–2.0 |

directly used as the electrodes without any conductive agent and binders. The control samples of bulk $WS_2$ powder (~99%, by Sigma-Aldrich) was mixed with conductive active carbon black and polyvinylidene fluoride (PVDF) in the weight ratio of 8 : 1 : 1. The above powders were mixed with *N*-methyl-pyrrolidone (NMP) in a mortar agate to prepare a homogenous slurry. The resultant mixture appeared to be dark greyish slurry and applied directly onto nickel foam substrates and baked in a vacuum oven at 120 °C for more than 12 h to form pure $WS_2$ working electrodes. Another control sample is 3Dgn substrate without further deposition. In a typical assembly process, all working electrodes mentioned before were assembled into a CR2032 coin cells with a Celgard 2400 membrane as a separator. 1 M of $LiPF_6$ dissolved in ethylene-carbonate–ethyl-methyl-carbonate (EC–DMC, 1 : 1) was used as the electrolyte for the assembly. All electrodes were assembled in an inert glove-box enclosure filled with argon gas with the oxygen and moisture level both controlled at lower than 1 ppm. The galvanostatic charge/discharge measurements were carried out in the voltage range of 0.01–3.00 V at current densities ranging from 100 mA $g^{-1}$ to 1500 mA $g^{-1}$ on a battery tester (Neware, Shenzhen, China). Cyclic voltammetry (CV) and electrochemical impedance spectroscopy (EIS) were carried out on an electrochemical workstation (VMP3 Bio-logic, France).

## 3. Results and discussion

### 3.1 Morphology and structure of $WS_2$–3Dgn nanocomposites

Fig. 1(a) shows the schematics of the nucleation process of $WS_2$ on 3Dgn at various plasma treatment times. When the 3Dgn is treated with 30 s of plasma (for the case of 30WSG) as shown in the SEM images in Fig. 1(b) and (c), the functionalized groups on graphene surface are activated as nucleation sites for the growth of $WS_2$ nanoparticles/island with an average growth diameter of less than 50 nm. The nanoparticles are uniformly distributed on the surface of the 3Dgn. The growth of $WS_2$ nanoparticles/island at the grain boundaries of 3Dgn is much bigger and agglomerated as usually there are more functional groups created at the grain boundaries than the center of graphene surface.[43] With the increase of the plasma treatment time to 60 s (60WSG), the activated nucleation sites are denser and subsequently more $WS_2$ nanoparticles are able to grow and interconnect adjacently to form a thin layered $WS_2$ nanoflakes

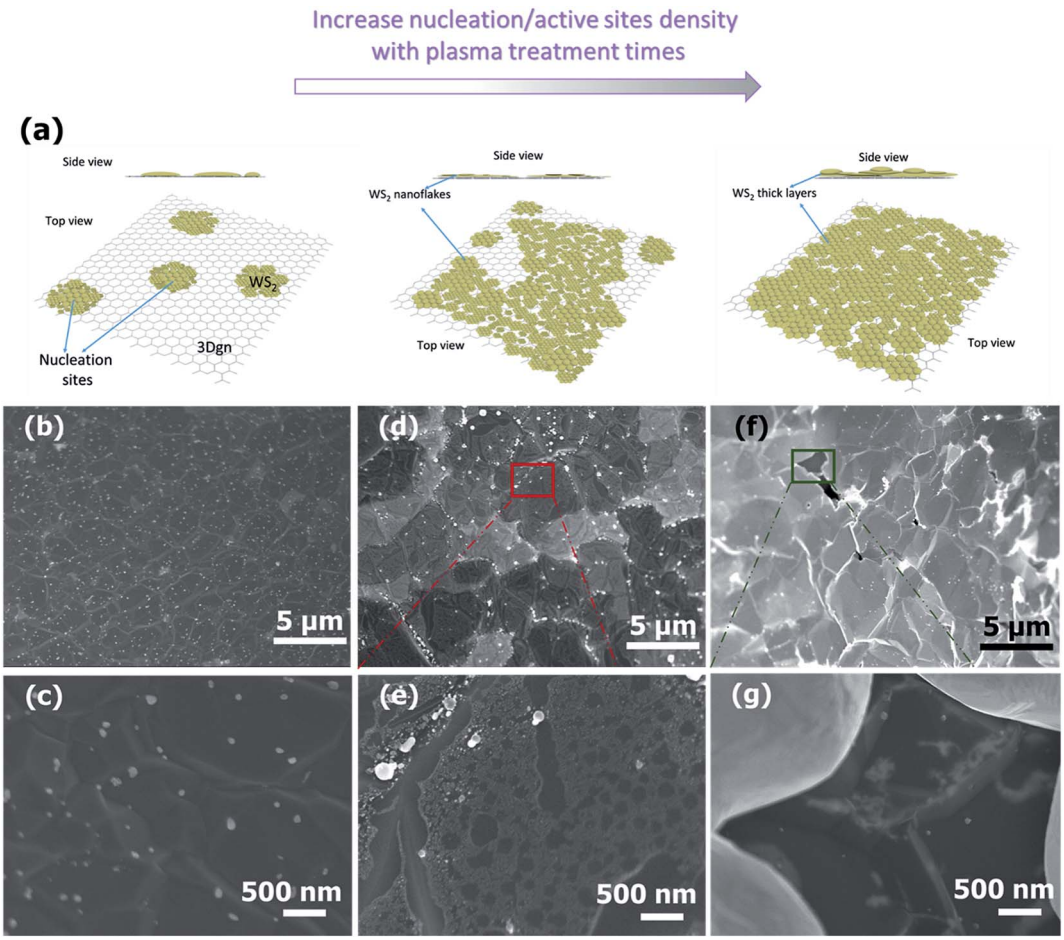


Fig. 1 (a) Schematic diagram of the morphological differences of the growth of $WS_2$ on 3Dgn from nanoparticles nucleation/island (30WSG), to nanoflakes (60WSG) and ultimately to $WS_2$ thick layers (90WSG) with increasing plasma treatment times. SEM images with various magnifications of (b) and (c) 30WSG, (d) and (e), 60WSG and (f) and (g) 90WSG $WS_2$–3Dgn nanocomposites.

 

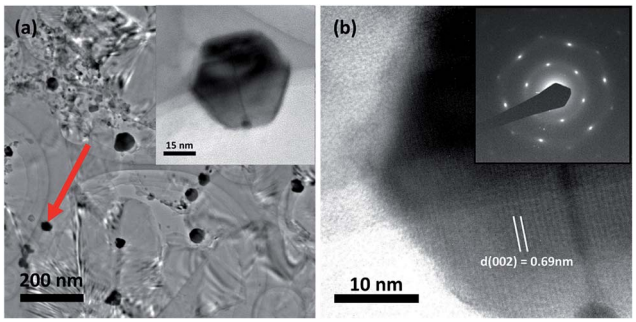


Fig. 2 (a) TEM and (b) HR-TEM images of the $WS_2$–3Dgn nanocomposites.

on the 3Dgn networks as shown in Fig. 1(d) and (e). Energy dispersive X-ray spectroscopy (EDS) mapping of the 60WSG-$WS_2$–3Dgn nanocomposites with the elements distribution is displayed in Fig. S1.† It is clearly see that W and S elements are distributed in the same position. This confirms the chemical composition of the $WS_2$ nanoflakes on 3Dgn. With the increase of plasma treatment duration to 90 s (90WSG), the growth of the $WS_2$ are assisted and motivated by the abundances of nucleation sites of which the layered structure is grown into a thicker (*i.e.*, bulk-like) appearance covering the 3Dgn surface as shown in Fig. 1(f) and (g). In comparison, the morphology of bulk $WS_2$ and pristine 3Dgn are shown in Fig. S2 and S3† respectively.

TEM characterization was employed to study the detailed nanostructure of $WS_2$ nanoparticles/nanoflakes on the graphene sheets. As shown in Fig. 2(a), $WS_2$ nanoflakes are grown onto the graphene sheets to form a stable structure, consistent with the SEM results. The bonding between $WS_2$ nanoflakes and 3Dgn is due to the van der Waal's forces and/or weak covalent bonding.[60,65,66] As shown in Fig. 2(b), high-resolution TEM (HR-TEM) and selected area electron diffraction (SAED) patterns confirm the crystalline structure of the $WS_2$ nanoflakes with the lattice spacing ($d$) of 0.69 nm corresponds to the (002) facial plane of $WS_2$.[44]

Fig. 3(a) depicts the XRD patterns of the pristine 3Dgn, pure commercial $WS_2$ powders and $WS_2$–3Dgn nanocomposites. The peaks at 14.364, 28.959, 32.769, 33.587, 39.600, 44.055, 49.800, 57.495, 60.010 and 60.600° are corresponding to the $WS_2$ crystal facial of (002), (004), (100), (101), (103), (006), (105), (110), (008) and (112), respectively. All peaks agreed well with the commercial $WS_2$ powder and standard powder diffraction card of JCPDS-841398 as well as previous reports.[45,46] The peak at 26.4°, which corresponds to that of the graphitic carbon of (002) plane (JCPDS-751621), is also observed on the $WS_2$–3Dgn nanocomposites (indicated by ○).[41] This peak can be associated to that of 3Dgn as shown in the XRD profile of the pristine 3Dgn. The sharp peaks located at 44.45, 51.71 and 76.41° belong to nickel metal from the nickel foam substrates.[47] No other significant patterns that belongs to other phases or compounds are observed. The $WS_2$–3Dgn nanocomposites were further characterized by Raman spectroscopy as shown in Fig. 3(b). The peaks located at 352 and 417 $cm^{-1}$ are corresponding to the vibrational modes of $E^1_{2g}(\Gamma)$ and $A_{1g}(\Gamma)$ of $WS_2$, respectively.[48] It is interesting to note that the intensity ratio $I(E^1_{2g})/I(A_{1g})$ changes with various composites owing to the thickness variation of $WS_2$ layers which agrees with previous studies.[49] The D band (1350 $cm^{-1}$) and G band (1580 $cm^{-1}$) of 3Dgn are also observed in the $WS_2$–3Dgn nanocomposites and pristine 3Dgn. They are corresponding to the (i) disordered $sp^2$-hybridisation of the graphene structure, and (ii) the graphene vibrational modes $E_{2g}(\Gamma)$ of the carbon covalent bonds in the graphene lateral planes, respectively.[50]

### 3.2 Electrochemical performance of $WS_2$–3Dgn nanocomposites

The electrochemical performance of $WS_2$–3Dgn nanocomposites (60WSG) were investigated by cyclic voltammetry (CV) in the range of 0.01 to 3.00 V (*vs.* $Li/Li^+$), as shown in Fig. 4(a). During the first cycle, the cathodic reaction at the broad range from 0.2 to 1.0 V can be ascribed to (i) the insertion of lithium ions into $WS_2$ crystal structure, (ii) the conversion reaction of $WS_2$ into W nanoparticles embedded in $Li_2S$ matrix, and (iii) the irreversible decomposition of the electrolyte leading to the formation of SEI film.[51,52] The same peak is also observed for the bulk $WS_2$ as shown in Fig. S4(a).† The reaction (1) can be denoted as follows,

$$WS_2 + 4Li^+ \rightarrow W + 2Li_2S \quad (1)$$

In the first anodic region, two distinctive peaks are observed at 1.9 and 2.4 V. The first peak at 1.9 V can be attributed to the

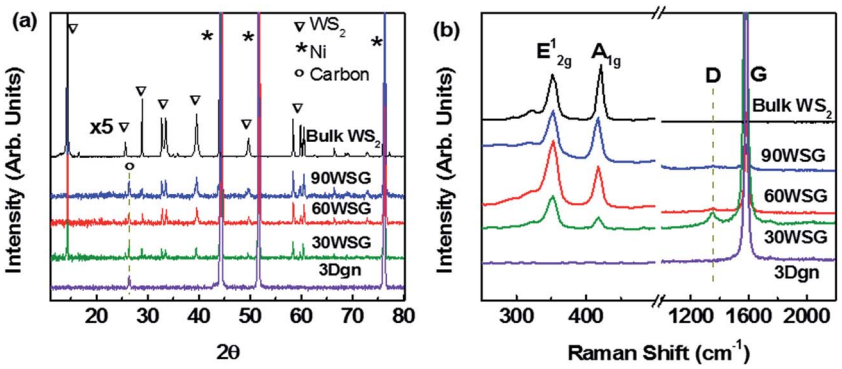


Fig. 3 (a) XRD patterns and (b) Raman spectra of 3Dgn, 30WSG, 60WSG and 90WSG $WS_2$–3Dgn nanocomposites and pure bulk $WS_2$ electrodes.

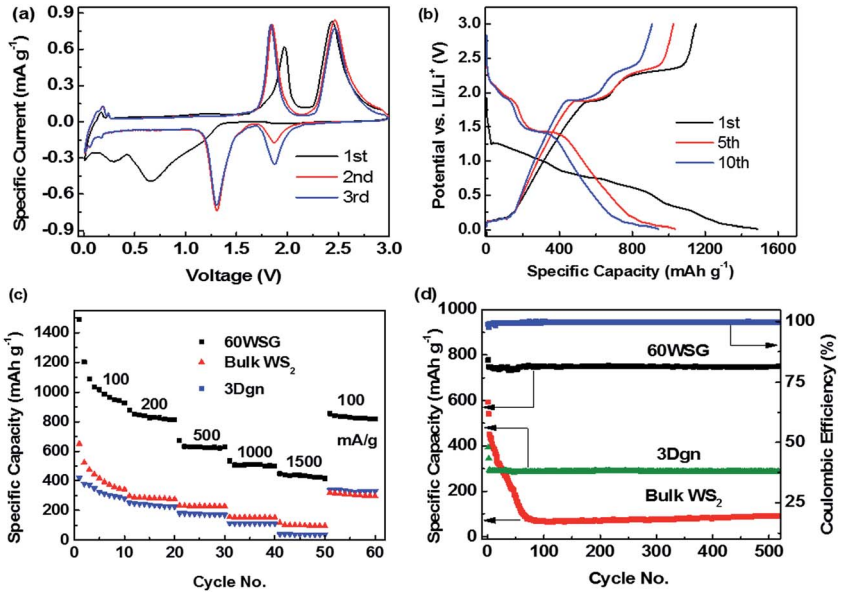


Fig. 4 (a) CV curves of the 60WSG $WS_2$–3Dgn nanocomposites of the first 3 cycles in the potential range of 0.01–3.00 V *vs.* $Li/Li^+$. (b) The galvanostatic charge and discharge profiles of the 60WSG $WS_2$–3Dgn composites of 1st, 5th and 10th cycles measured at a current density of 100 mA $g^{-1}$. (c) Rate capability (delithiation capacity) of the 60WSG $WS_2$–3Dgn nanocomposites, commercial $WS_2$ powder electrodes and pristine 3Dgn electrodes at the current densities of 100, 200, 500, 1000, 1500 mA $g^{-1}$. (d) Cycling performance of the 60WSG $WS_2$–3Dgn nanocomposites, bulk $WS_2$ and pristine 3Dgn at a current density of 200 mA $g^{-1}$, and Coulombic Efficiency of 60WSG $WS_2$–3Dgn nanocomposites electrode.

interaction of $Li_2S$ to the metal tungsten nanoparticles (reaction (2)). For the case of bulk $WS_2$ based electrodes, this reaction is not readily available due to the $Li_2S$ generated in the first reaction are not effectively reacting with the metal in the bulk matrix, as confirmed in the CV of the bulk $WS_2$ electrode as shown in Fig. S4(a).†[53]

$$2Li_2S + W \rightarrow 2xLi^+ + WS_x + 2xe^- \quad (2)$$

The anodic peak at 2.4 V is attributed to the oxidation of $Li_2S$ to S, which expressed as the reaction below (forward reaction of reaction (3)).[54]

$$2Li_2S \leftrightarrow 4Li^+ + S_2^{2-} + 2e^- \quad (3)$$

The anodic and cathodic profiles of the $WS_2$–3Dgn nanocomposites at the lower voltage range of 0.01–0.25 V is ascribed to the characteristic reaction of the $Li_xC$ insertion/extraction of Li-ion processes into the graphene layers.[55–57] This is confirmed by the comparison with the CV profiles of the pristine 3Dgn as shown in Fig. S5(a).†

For the subsequent cycles (2nd and 3rd cycles), two distinctive reduction peaks located at 1.25 and 1.8 V are attributed to the lithium insertion into the crystal structure of $WS_2$ following equation as shown (forward reaction of reaction (4)).[25,58]

$$WS_2 + xLi^+ + xe^- \leftrightarrow Li_xWS_2 \quad (4)$$

For the anodic region, apart from the higher voltage region of 2.4 V (reaction (3) of the sulfurization peak), the anodic peak at 1.9 V is also observed and is higher in comparison to the 1st cycle. This indicates more contribution from reaction (2). This also indicates that reaction (2) are sustained in subsequent cycles. It has been reported that this reaction is responsible of having the impact and significance of producing highly stable and excellent rate capacity due to the higher irreversibility of reaction (2) compared to the reaction (3), which only reaction (3) is usually observed in the bulk $WS_2$ electrodes.[53]

Fig. 4(b) shows the 1st, 5th and 10th galvanostatic charge/discharge curves of the 60WSG $WS_2$–3Dgn nanocomposites at current density of 100 mA $g^{-1}$. During the first discharge cycle, a broad plateau is observed at around 0.75 V. The reaction corresponds to the lithium intercalation reaction accompanied by the formation of the SEI layer.[58] For the charging processes, two plateaus at 1.9 and 2.4 V are ascribed to the reaction of $Li_2S$ to the metallic W into $WS_2$ as well as the oxidation of $Li_2S$ respectively.[53] For the subsequent discharging cycles, this first reduction plateau diminishes and two distinctive new reduction plateaus appear at 1.9 and 1.4 V which can be ascribed to the lithiation process.[24,27] The galvanostatic charge and discharge of 30WSG and 90WSG display the same profiles and are shown in Fig. S6(b) and S7(b)† respectively. Interestingly for the 60WSG-$WS_2$–3Dgn nanocomposites, the 1st cycle charge and discharge capacities are 1150 and 1480 mA h $g^{-1}$, respectively, leading to a high first cycle Coulombic Efficiency (CE) of 77% that is higher than most reported $WS_2$ based electrode materials.[25,44,58] In the 2nd cycle, the charge and discharge capacities are 1080 and 1202 mA h $g^{-1}$, respectively with an increase of CE to 90%. The CE remained higher than 98% for subsequent and longer cycles. The high CE indicates that the active ions in the $WS_2$–3Dgn nanocomposites electrodes participating the lithiation/delithiation are highly reversible and with low energy loss.

 

The rate capabilities of all electrodes were tested under various current densities ranging from 100, 200, 500, 1000 and 1500 mA $g^{-1}$. Remarkably, the 60WSG-$WS_2$–3Dgn nanocomposites are able to deliver specific capacities of 927, 815, 630, 500, 416 mA h $g^{-1}$ at the current densities of 100, 200, 500, 1000 and 1500 mA $g^{-1}$, respectively, as shown in Fig. 4(c). The rate capability of 30WSG and 90WSG-$WS_2$–3Dgn nanocomposites were shown in Fig. S8.† It is worth mentioning that for the 60WSG composites, the specific capacity returned to 820 mA h $g^{-1}$ when the current density is adjusted from 1500 to 100 mA $g^{-1}$. In contrast, the specific capacities of $WS_2$–3Dgn nanocomposites are much higher than that of bulk $WS_2$ and pure 3Dgn especially at the higher current densities. The bulk $WS_2$ powder and 3Dgn only deliver specific capacities of 152 and 112 mA h $g^{-1}$ at a current density of 1000 mA $g^{-1}$, respectively. It is also notable that the capacity of bulk $WS_2$ decreases quickly with increasing current densities. This indicates the superior rate capability of the $WS_2$–3Dgn nanocomposites in contrast to that of the bulk $WS_2$ and the pristine 3Dgn electrodes.

The cycling performance of the $WS_2$–3Dgn nanocomposites, bulk $WS_2$ and pristine 3Dgn at a current density of 200 mA $g^{-1}$ are shown in Fig. 4(d). The $WS_2$–3Dgn nanocomposites exhibit stable cycle performance and deliver a remarkable specific capacity of 748 mA h $g^{-1}$ after 500 cycles. Although the pristine 3Dgn also shows stable cycle performance, it only can deliver a capacity of 287 mA h $g^{-1}$ after 500 cycles at the same current density. The specific capacity of bulk $WS_2$ reduces rapidly from 541 at the 1$^{st}$ discharge cycle to 90 mA h $g^{-1}$ after 100 cycles at the same current density. Thus, with the incorporation of $WS_2$ nanoflakes onto 3Dgn, the specific capacity as well as the cycling performance of the $WS_2$ are greatly improved. We also note that the cycling performance is also affected by the loading of $WS_2$. For the case of 30WSG nanocomposites as shown in Fig. S9(a),† the cycling stability is able to maintain a relative lower specific capacity of 324 mA h $g^{-1}$ even after 500 cycles. For the case of 90WSG nanocomposites, they exhibit a high specific capacity of 638 mA h $g^{-1}$ at the 1$^{st}$ cycle, but degrade to 240 mA h $g^{-1}$ after 100 cycles as shown in Fig. S9(b).† It is also worth mentioning that the $WS_2$–3Dgn nanocomposites are able to retain its morphology after 500 cycles at 200 mA $g^{-1}$ showing remarkable robustness of $WS_2$ layers with 3Dgn as backbone under lithiation/delithiation cycles, as shown in Fig. S10.†

In order to explore intrinsic electrochemical kinetics of the $WS_2$–3Dgn nanocomposites, electrochemical impedance spectroscopy (EIS) were conducted over the frequency range of 10 mHz to 1 MHz as shown in Fig. 5. The Nyquist diagram or the EIS diagram were fitted using the circuitry model as depicted in the inset of Fig. 5(a). $R_s$ represents the current collector and electrolyte resistance; $R_f$ and $Q_1$ represent SEI layer resistance and the constant phase element (CPE) respectively; $R_{ct}$ and $Q_2$ represent charge transfer resistance and double layer capacitor, respectively. $Z_w$ represents the Warburg impedance related to the lithium diffusion.[59] The fitted results are summarized in Table 2. The results show that with the incorporation of the 3Dgn to the $WS_2$, the charge transfer resistance of the $WS_2$–3Dgn composite electrodes (from 116, 156.70 to 241.80 Ω with increasing $WS_2$ mass loadings) is significantly smaller than that of the pure bulk $WS_2$ electrodes (784.60 Ω).

The excellent performance of the $WS_2$–3Dgn composites in comparison to the bulk $WS_2$ electrodes are attributed to the rational design of the $WS_2$–3Dgn nanostructure and the synergistic effect between 3Dgn network and $WS_2$ nanoflakes, of which the incorporation are assisted by the plasma treatment prior to nanoflakes growth: (1) $WS_2$ nanoflakes have provided large surface area with shortened lithium ion diffusion path compared to that of bulk $WS_2$. (2) $WS_2$–3Dgn composites were shown to have better structure retainability due to mechanically robust 3Dgn backbone during the lithiation/delithiation process. (3) 3Dgn provides excellent electric conductivity to reduce the resistance of the $WS_2$ layers (charge resistance is

Table 2 Fitting results of the EIS spectra with the configurative circuitry model as shown in Fig. 5(a)

| Sample | $R_s$ (Ω) | $R_f$ (Ω) | $R_{ct}$ (Ω) |
|---|---|---|---|
| Bulk $WS_2$ | 14.35 | 745.6 | 784.6 |
| 3Dgn | 22.10 | 81.13 | 68.52 |
| 30WSG | 24.35 | 92.89 | 116.0 |
| 60WSG | 15.89 | 118.62 | 156.7 |
| 90WSG | 18.31 | 133.67 | 241.80 |

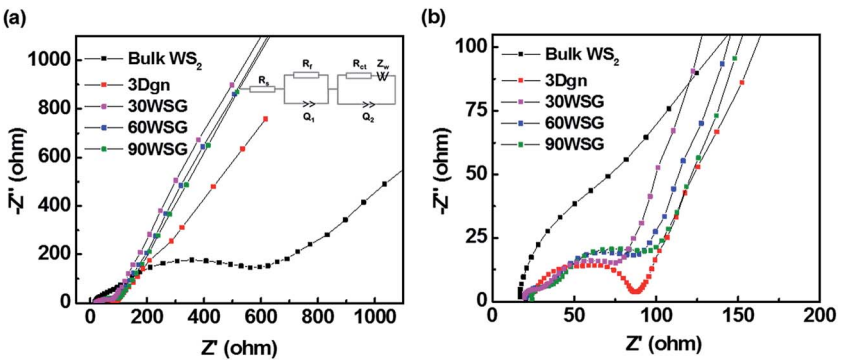


Fig. 5 Nyquist impedance spectra of the bulk $WS_2$, 3Dgn and $WS_2$–3Dgn nanocomposites. (a) in the full range of $Z'$ and $-Z''$ from 0 to 1000 Ω. Inset shows the model for the EIS test circuit. (b) In region of $Z'$ and $-Z''$ from 0 to 200 Ω.

reduced with the incorporation of 3Dgn as shown in EIS data).[65] This enhancement is more prominent in particularly for the case of the low mass loading samples (*i.e.* 30WSG and 60WSG). (4) The binder free structure during cell assembly further improves the lithium-ion/$WS_2$–3Dgn nanostructure behavior without causing unneeded increase of resistance. As LIBs anode materials, these results indicate that $WS_2$–3Dgn nanocomposites exhibit superior and excellent specific capacities, rate capabilities as well as stable cycling as compare to the pure bulk $WS_2$ electrodes.

## 4. Conclusion

In summary, $WS_2$–3Dgn hybrid nanocomposites were synthesized by a simple CVD method. $WS_2$ nanoparticles/nanoflakes are uniformly grown on the surface of 3Dgn networks. 3Dgn network not only provide the template for the growth of $WS_2$ nanostructures, but also increase the conductivity of $WS_2$ during the lithiation/delithiation processes. As LIBs electrode materials, $WS_2$–3Dgn nanocomposites exhibit excellent electrochemical performance, with superior specific capacity, rate capabilities and more stable cycling performance as compared to the bulk $WS_2$ electrodes. The outstanding performance is due to synergistic effect of the pristine three dimensional graphene network supporting the electrochemical reaction of $WS_2$ in both mechanically and electronically. By incorporation of $WS_2$ to 3Dgn which the growth mechanism and the electrochemical performance can be controlled *via* plasma activation to 3Dgn, this work opens up a new yet simple to use method in optimizing electrochemical performance of TMDs in its application as LIBs anode materials.

## Acknowledgements

This research is supported by the National Research Foundation, Prime Minister's Office, Singapore under its NRF-ANR Joint Grant Call (NRF-ANR Award No. NRF2015-NRF-ANR000-CEENEMA).

## References

1 M. Armand and J.-M. Tarascon, *Nature*, 2008, **451**, 652–657.
2 J.-M. Tarascon and M. Armand, *Nature*, 2001, **414**, 359–367.
3 B. Dunn, H. Kamath and J.-M. Tarascon, *Science*, 2011, **334**, 928–935.
4 A. S. Aricò, P. Bruce, B. Scrosati, J.-M. Tarascon and W. van Schalkwijk, *Nat. Mater.*, 2005, **4**, 366–377.
5 B. Lung-Hao Hu, F.-Y. Wu, C.-T. Lin, A. N. Khlobystov and L.-J. Li, *Nat. Commun.*, 2013, **4**, 1687.
6 D. Larcher and J.-M. Tarascon, *Nat. Chem.*, 2014, **7**, 19–29.
7 B. Scrosati, *Electrochim. Acta*, 2000, **45**, 2461–2466.
8 K. Kang, Y. S. Meng, J. Bréger, C. P. Grey and G. Ceder, *Science*, 2006, **311**, 977–980.
9 F. Cheng, J. Liang, Z. Tao and J. Chen, *Adv. Mater.*, 2011, **23**, 1695–1715.
10 A. Manthiram, *J. Phys. Chem. Lett.*, 2011, **2**, 176–184.
11 X. Chia, A. Y. S. Eng, A. Ambrosi, S. M. Tan and M. Pumera, *Chem. Rev.*, 2015, **115**, 11941–11966.
12 J. B. Goodenough and Y. Kim, *Chem. Mater.*, 2010, **22**, 587–603.
13 J. Xiao, W. Xu, D. Wang, D. Choi, W. Wang, X. Li, G. L. Graff, J. Liu and J.-G. Zhang, *J. Electrochem. Soc.*, 2010, **157**, A1047–A1051.
14 J. Chen, N. Kuriyama, H. Yuan, H. T. Takeshita and T. Sakai, *J. Am. Chem. Soc.*, 2001, **123**, 11813–11814.
15 P. G. Bruce, S. A. Freunberger, L. J. Hardwick and J.-M. Tarascon, *Nat. Mater.*, 2011, **11**, 19–29.
16 X. Rui, H. Tan and Q. Yan, *Nanoscale*, 2014, **6**, 9889–9924.
17 M. Tatsumisago, S. Hama, A. Hayashi, H. Morimoto and T. Minami, *Solid State Ionics*, 2002, **154**, 635–640.
18 V. K. Deshpande, A. Pradel and M. Ribes, *Solid State Ionics*, 1988, **28–30**, 756–761.
19 Y. Wang, B. Chen, D. H. Seo, Z. J. Han, J. I. Wong, K. Ostrikov, H. Zhang and H. Y. Yang, *NPG Asia Mater.*, 2016, **8**, e268.
20 Y. Wang, D. Kong, W. Shi, B. Liu, G. J. Sim, Q. Ge and H. Y. Yang, *Adv. Energy Mater.*, 2016, **6**, 1601057.
21 R. Chen, T. Zhao, W. Wu, F. Wu, L. Li, J. Qian, R. Xu, H. Wu, H. M. Albishri, A. S. Al-Bogami, D. A. El-Hady, J. Lu and K. Amine, *Nano Lett.*, 2014, **14**, 5899–5904.
22 C. Feng, L. Huang, Z. Guo and H. Liu, *Electrochem. commun.*, 2007, **9**, 119–122.
23 C. S. Reddy, A. Zak and E. Zussman, *J. Mater. Chem.*, 2011, **21**, 16086–16093.
24 H. Li, K. Yu, H. Fu, B. Guo, X. Lei and Z. Zhu, *Phys. Chem. Chem. Phys.*, 2015, **17**, 29824–29833.
25 X. Xu, C. S. Rout, J. Yang, R. Cao, P. Oh, H. S. Shin and J. Cho, *J. Mater. Chem. A*, 2013, **1**, 14548–14554.
26 D. Chen, G. Ji, B. Ding, Y. Ma, B. Qu, W. Chen and J. Y. Lee, *Nanoscale*, 2013, **5**, 7890–7896.
27 S. Yu, J.-W. Jung and I.-D. Kim, *Nanoscale*, 2015, **7**, 11945–11950.
28 Z.-S. Wu, G. Zhou, L.-C. Yin, W. Ren, F. Li and H.-M. Cheng, *Nano Energy*, 2012, **1**, 107–131.
29 C. Liu, F. Li, L.-P. Ma and H.-M. Cheng, *Adv. Mater.*, 2010, **22**, E28–E62.
30 H. Wang, J. T. Robinson, X. Li and H. Dai, *J. Am. Chem. Soc.*, 2009, **131**, 9910–9911.
31 Z. Chen, W. Ren, L. Gao, B. Liu, S. Pei and H.-M. Cheng, *Nat. Mater.*, 2011, **10**, 424–428.
32 X. Cao, Y. Shi, W. Shi, X. Rui, Q. Yan, J. Kong and H. Zhang, *Small*, 2013, **9**, 3433–3438.
33 S. Mao, G. Lu and J. Chen, *Nanoscale*, 2015, **7**, 6924–6943.
34 Y. Ma and Y. Chen, *Natl. Sci. Rev.*, 2015, **2**, 40–53.
35 A. K. Geim and K. S. Novoselov, *Nat. Mater.*, 2007, **6**, 183–191.
36 Q. H. Wang and M. C. Hersam, *Nat. Chem.*, 2009, **1**, 206–211.
37 Y. Si and E. T. Samulski, *Nano Lett.*, 2008, **8**, 1679–1682.
38 B. Li, L. Zhou, D. Wu, H. Peng, K. Yan, Y. Zhou and Z. Liu, *ACS Nano*, 2011, **5**, 5957–5961.
39 J. T. Robinson, J. S. Burgess, C. E. Junkermeier, S. C. Badescu, T. L. Reinecke, F. K. Perkins, M. K. Zalalutdniov, J. W. Baldwin, J. C. Culbertson, P. E. Sheehan and E. S. Snow, *Nano Lett.*, 2010, **10**, 3001–3005.

 

40 G. Bruno, G. V. Bianco, M. M. Giangregorio, M. Losurdo and P. Capezzuto, *Phys. Chem. Chem. Phys.*, 2014, **16**, 13948–13955.
41 Z. X. Huang, Y. Wang, Y. G. Zhu, Y. Shi, J. I. Wong and H. Y. Yang, *Nanoscale*, 2014, **6**, 9839–9845.
42 D. Hunyadi, A. L. Vieira Machado Ramos and I. M. Szilágyi, *J. Therm. Anal. Calorim.*, 2015, **120**, 209–215.
43 M. Seifert, J. E. B. Vargas, M. Bobinger, M. Sachsenhauser, A. W. Cummings, S. Roche and J. A. Garrido, *2D Mater.*, 2015, **2**, 024008.
44 K. Shiva, H. S. S. Ramakrishna Matte, H. B. Rajendra, A. J. Bhattacharyya and C. N. R. Rao, *Nano Energy*, 2013, **2**, 787–793.
45 Y. Feldman, G. L. Frey, M. Homyonfer, V. Lyakhovitskaya, L. Margulis, H. Cohen, G. Hodes, J. L. Hutchison and R. Tenne, *J. Am. Chem. Soc.*, 1996, **118**, 5362–5367.
46 C. Luhrs, M. Moberg, A. Maxson, L. Brewer and S. Menon, *Inorganics*, 2014, **2**, 211–232.
47 A. Ul-Hamid, A. Quddus, H. Saricimen, H. Dafalla, A. Ul-Hamid, A. Quddus, H. Saricimen and H. Dafalla, *Mater. Res.*, 2015, **18**, 20–26.
48 H. S. S. Ramakrishna Matte, A. Gomathi, A. K. Manna, D. J. Late, R. Datta, S. K. Pati and C. N. R. Rao, *Angew. Chem., Int. Ed.*, 2010, **49**, 4059–4062.
49 A. Berkdemir, H. R. Gutiérrez, A. R. Botello-Méndez, N. Perea-López, A. L. Elías, C.-I. Chia, B. Wang, V. H. Crespi, F. López-Urías, J.-C. Charlier, H. Terrones and M. Terrones, *Sci. Rep.*, 2013, **3**, 1755.
50 A. C. Ferrari, J. C. Meyer, V. Scardaci, C. Casiraghi, M. Lazzeri, F. Mauri, S. Piscanec, D. Jiang, K. S. Novoselov, S. Roth and A. K. Geim, *Phys. Rev. Lett.*, 2006, **97**, 187401.
51 Q. Wang and J. Li, *J. Phys. Chem. C*, 2007, **111**, 1675–1682.
52 G. X. Wang, S. Bewlay, J. Yao, H.-K. Liu, S. X. Dou, S. Bewlay, J. Yao and H. K. Liu, *Electrochem. Solid-State Lett.*, 2004, **7**, 321–323.
53 X. Li, J. Zai, S. Xiang, Y. Liu, X. He, Z. Xu, K. Wang, Z. Ma and X. Qian, *Adv. Energy Mater.*, 2016, **6**, 1601056.
54 Y. Liu, W. Wang, H. Huang, L. Gu, Y. Wang and X. Peng, *Chem. Commun.*, 2014, **50**, 4485–4488.
55 F. Ding, W. Xu, D. Choi, W. Wang, X. Li, M. H. Engelhard, X. Chen, Z. Yang and J.-G. Zhang, *J. Mater. Chem.*, 2012, **22**, 12745–12751.
56 P. Han, W. Ma, S. Pang, Q. Kong, J. Yao, C. Bi and G. Cui, *J. Mater. Chem. A*, 2013, **1**, 5949–5954.
57 J. Wang, C. Feng, Z. Sun, S. Chou, H. Liu and J. Wang, *Sci. Rep.*, 2014, **4**, 7030.
58 H. Liu, D. Su, G. Wang and S. Z. Qiao, *J. Mater. Chem.*, 2012, **22**, 17437–17440.
59 Y. Wang, Z. J. Han, S. F. Yu, R. R. Song, H. H. Song, K. Ostrikov and H. Y. Yang, *Carbon*, 2013, **64**, 230–236.
60 T. Ahmed, N. A. Modine and J.-X. Zhu, *Appl. Phys. Lett.*, 2015, **107**, 043903.
61 B. Li, M. Zheng, H. Xue and H. Pang, *Inorg. Chem. Front.*, 2016, **3**, 175–202.
62 Y. Yan, B. Li, W. Guo, H. Pang and H. Xue, *J. Power Sources*, 2016, **329**, 148–169.
63 Y. Yan, H. Xu, W. Guo, Q. Huang, M. Zheng, H. Pang and H. Xue, *Inorg. Chem. Front.*, 2016, **3**, 791–797.
64 H. Pang, Y. Zhang, W.-Y. Lai, Z. Hu and W. Huang, *Nano Energy*, 2015, **15**, 303–312.
65 E. G. S. Firmiano, A. C. Rabelo, C. J. Dalmaschio, A. N. Pinheiro, E. C. Pereira, W. H. Schreiner and E. R. Leite, *Adv. Energy Mater.*, 2014, **4**, 1301380.
66 Y. D. Ma, Y. Dai, M. Guo, C. W. Niu and B. B. Huang, *Nanoscale*, 2011, **3**, 3883–3887.